Fault classification and location using HS-transform and radial basis function neural network

S.R. Samantaray [a,*], P.K. Dash [b,1], G. Panda [a,1]

[a] *National Institute of Technology, Rourkela, India*
[b] *College of Engineering, Bhubaneswar, India*

Abstract

A new approach for protection of transmission lines has been presented in this paper. The proposed technique consists of preprocessing the fault current and voltage signal sample using hyperbolic S-transform (HS-transform) to yield the change in energy and standard deviation at the appropriate window variation. After extracting these two features, a decision of fault or no-fault on any phase or multiple phases of the transmission line is detected, classified, and its distance to the relaying point found out using radial basis function neural network (RBFNN) with recursive least square (RLS) algorithm. The ground detection is done by a proposed indicator '*index*'. As HS-transform is very less sensitive to noise compared to wavelet transform, the proposed method provides very accurate and robust relaying scheme for distance protection.

Keywords: Distance protection; Energy change calculations; HS-transform; RBFNN

1. Introduction

Different types of transient phenomena occur on the transmission line. From these transient phenomena, faults on transmission lines need to be detected, classified, located accurately, and cleared as fast as possible. In power transmission line protection, faulty phase identification and location of fault are the two most important items which need to be addressed in a reliable and accurate manner. Distance relaying techniques based on the measurement of the impedance at the fundamental frequency between the fault location and the relaying point have attracted wide spread attention. The sampled voltage and current data at the relying point are used to locate and classify the fault involving the line with or without fault resistance present in the fault path.

The accuracy of the fault classification and location also depends on the amplitude of the dc offset and harmonics in comparison to the fundamental component. Fourier transforms, differential equations, waveform modeling and Kalman filters, and wavelet transforms are some of the techniques used for fault detection and location calculation [1–6]. Some of the recent papers in this area [3,4,6] have used only the sampled current values at the relaying point during faults for classification of fault types and distance calculations.

In recent years, neural networks are trained to recognize fault patterns associated with the voltage and current waveforms from the relaying point due to their superior ability to learn and generalize from training patterns. However, in the fault classification and location tasks, the neural networks cannot produce accurate results due to the inaccuracies in the input phasor data and the requirement of a large number of neural networks for different categories of fault.

Another pattern recognition technique based on wavelet transform has been found to be an effective tool in monitoring and analyzing power system disturbances including power quality assessment [13] and system protection against faults. Although wavelets provide a variable window for low and high frequency currents in the voltage and current waveforms during faults, their capabilities are often significantly degraded owing to the existence of noises riding high on the signal [7]. In particular, as the spectrum of the noises coincides with that of the transient signals, the effects of noises cannot be excluded by means of some kinds of filters without affecting the performance of the wavelet transform. Another powerful time–frequency anal-

* Corresponding author. Tel.: +91 9437108895; fax: +91 674 2725312.
E-mail address: sbh_samant@rediffmail.com (S.R. Samantaray)

ysis known as S-transform has found applications in geoscience and power engineering [8–10]. The S-transform is an invertible time–frequency spectral localization technique that combines elements of wavelet transforms and short-time Fourier transform. The S-transform uses an analysis window whose width is decreasing with frequency providing a frequency dependent resolution. This transform may be seen as a continuous wavelet transform with a phase correction. It produces a constant relative bandwidth analysis like wavelets while it maintains a direct link with Fourier spectrum. The S-transform has an advantage in that it provides multi resolution analysis while retaining the absolute phase of each frequency. This has led to its application for detection and interpretation of events in a time series like the power quality disturbances [11].

The feature extraction from the faulted current signal, a variant of the original S-transform [12] is used where a pseudo-Gaussian hyperbolic window is used to provide better time and frequency resolutions at low and high frequencies unlike the S-transform using the Gaussian window. Here the hyperbolic window has frequency dependence in its shape in addition to its width and height. The increased asymmetry of the window at low frequencies leads to an increase in the width in the frequency domain, with consequent interference between major noise frequencies. In this paper the hyperbolic S-transform (HS-transform) is used to calculate the change in energy and standard deviation of the fault current and voltage signal which are fed to the RBFNN for fault classification and location determination from the relaying point. PSCAD package is used to generate fault data for varying location, fault resistance and inception angle and changed source impedance.

2. Hyperbolic S-transform for feature extraction

The original S-transform [8] is defined as

$$S(\tau, f) = \int_{-\infty}^{\infty} h(t) \left\{ \frac{|f|}{\sqrt{2\pi}} \exp\left\{ -\frac{f^2(\tau - t)}{2} \right\} \times \exp(-2\pi f t) \right\} \mathrm{d}t \tag{1}$$

where S denotes the S-transform of $h(t)$, which is the actual fault current or voltage signal varying with time, frequency is denoted by f, and the quantity τ is a parameter which controls the position of Gaussian window on the time-axis. A small modification of the Gaussian window has been suggested for better performance.

$$W_{\mathrm{gs}}(\tau - t, f, \alpha_{\mathrm{gs}}) = \frac{|f|}{\sqrt{2\pi\alpha_{\mathrm{gs}}}} \exp \frac{[-f^2(\tau - t)]}{2\alpha_{\mathrm{gs}}^2} \tag{2}$$

and the S-transform with this window is given by

$$S(\tau, f, \alpha_{\mathrm{gs}}) = \int_{-\infty}^{\infty} h(t)\omega(\tau - t, f, \alpha_{\mathrm{gs}}) \exp(-2\pi i f t)\, \mathrm{d}t \tag{3}$$

where α_{gs} is to be chosen for providing suitable time and frequency resolution.

In applications, which require simultaneous identification time–frequency signatures of different faulted phase currents and voltages, it may be advantageous to use a window having frequency dependent asymmetry. Thus, at high frequencies where the window is narrowed and time resolution is good, a more symmetrical window needs to be chosen. On the other hand, at low frequencies where a window is wider and frequency resolution is less critical, a more asymmetrical window may be used to prevent the event from appearing too far ahead on the S-transform. Thus an hyperbolic window of the form given below is used.

$$W_{\mathrm{hy}} = \frac{2|f|}{\sqrt{2\pi(\alpha_{\mathrm{hy}} + \beta_{\mathrm{hy}})}} \exp\left\{ \frac{-f^2 X^2}{2} \right\} \tag{4}$$

where

$$X = \frac{\alpha_{\mathrm{hy}} + \beta_{\mathrm{hy}}}{2\alpha_{\mathrm{hy}}\beta_{\mathrm{hy}}}(\tau - t - \xi) + \frac{\alpha_{\mathrm{hy}} - \beta_{\mathrm{hy}}}{2\alpha_{\mathrm{hy}}\beta_{\mathrm{hy}}} \sqrt{(\tau - t - \xi)^2 + \lambda_{\mathrm{hy}}^2} \tag{5}$$

In the above expression $0 < \alpha_{\mathrm{hy}} < \beta_{\mathrm{hy}}$ and ξ is defined as

$$\xi = \frac{\sqrt{(\beta_{\mathrm{hy}} - \alpha_{\mathrm{hy}})^2 \lambda_{\mathrm{hy}}^2}}{4\alpha_{\mathrm{hy}}\beta_{\mathrm{hy}}} \tag{6}$$

The translation by ξ ensures that the peak W_{hy} occurs at $\tau - t = 0$. At $f = 0$, W_{hy} is very asymmetrical, but when f increases, the shape of W_{hy} converges towards that of the symmetrical Gaussian window W_{gs} given in Eq. (2). For different values of α_{hy} and β_{hy} and with $\lambda_{\mathrm{hy}}^2 = 1$, Fig. 1 shows the nature of the window as the function of time $\tau - t$. As seen from the figure the change in the shape from an asymmetrical window to a symmetrical one occurs more rapidly with increasing f. The discrete version of the hyperbolic S-transform of the faulted voltage and current signal samples at the relaying point is calculated as

$$S[n, j] = \sum_{m=0}^{N-1} H[m + n]G(m, n) \exp(i2\pi m j) \tag{7}$$

where N is the total number of samples and the indices n, m, j are $n = 0, 1, \ldots, N-1$, $m = 0, 1, \ldots, N-1$ and $j = 0, 1, \ldots, N-1$.

The $G(m, n)$ denotes the Fourier transform of the hyperbolic window and is given by

$$G(m, n) = \frac{2|f|}{\sqrt{2\pi(\alpha_{\mathrm{hy}} + \beta_{\mathrm{hy}})}} \exp\left(\frac{-f^2 X^2}{2n^2} \right) \tag{8}$$

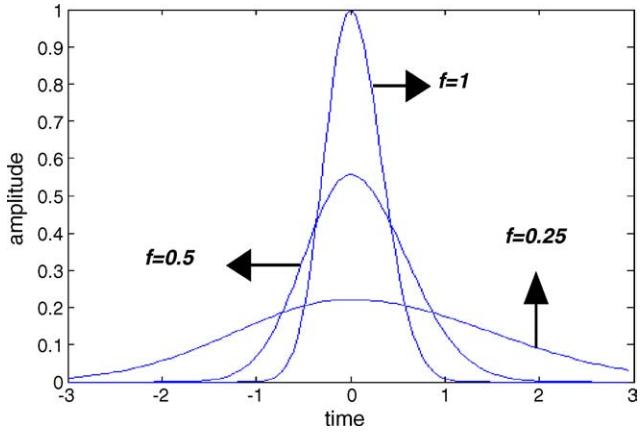

Fig. 1. Varying window W_{hy} at $f = 1$, 0.5, and 0.25.

here

$$X = \frac{(\alpha_{hy} + \beta_{hy})}{2\alpha_{hy}\beta_{hy}} t + \frac{\beta_{hy} - \alpha_{hy}}{2\alpha_{hy}\beta_{hy}} \left(\sqrt{t^2 + \lambda_{hy}} \right) \quad (9)$$

and $H(m, n)$ is the frequency shifted discrete Fourier transform $H[m]$ and is given by

$$H(m) = \frac{1}{N} \sum_{m=0}^{N-1} h(k) \exp(-i2\pi nk) \quad (10)$$

The computational steps of the hyperbolic S-transform are:

(i) $H[m]$ of the faulted voltage and current wave form samples are calculated and shifted to give $H[n + m]$;
(ii) the localizing hyperbolic Gaussian window $G[m, n]$ is evaluated;
(iii) $H[n + m]$ and $G[m, n]$ are multiplied and the inverse Fourier transform of the product is found out to give the rows of $S[n, j]$ corresponding to the frequency n.

The hyperbolic S-transform is found to be a complex matrix $S\left[\frac{N}{2}, N\right]$. Fig. 2 shows the flow chart for HS-transform.

3. System studied

The model network shown in Fig. 3 has been simulated using PSCAD (EMTDC) package. The network having two areas connected by the transmission line of 400 kV. The transmission line has zero sequence impedance $Z(0) = 96.45 + j335.26\ \Omega$ and positive sequence impedance $Z(1) = 9.78 + j110.23\ \Omega$ and $E_S = 400$ kV, $E_R = 400\angle\delta$ kV. The relaying point is as shown in Fig. 3, where data is retrieved for different conditions. Isolation of over voltage and high frequency components can be performed according to the required level of decomposition and reconstruction. The sampling rate is 1.0 kHz at 50 Hz base frequency. The change in energy and standard deviation are calculated from the S-transform of the current and voltage signal one cycle ahead and one cycle back from the fault inception. Fig. 4 shows the fault voltage and current signal for three phase fault. The proposed scheme is depicted as in Fig. 5.

4. Fault classification

4.1. Feature extraction

For faulty phase identification or fault classification only current signal is preprocessed through HS-transform to find out the features. The HS-transform outputs of the faulted current signal for different types of faults at 10–90% of the line with different incidence angles, source impedance and fault resistances are used to provide the following pertinent features, which can be used to classify the type of fault. Change in the signal energy and standard deviation of the HS-transform contour are obtained as

$$ce = E_f - E_A = \{abs(hs_f\}^2 - \{abs(hs_n\}^2 \quad (11)$$

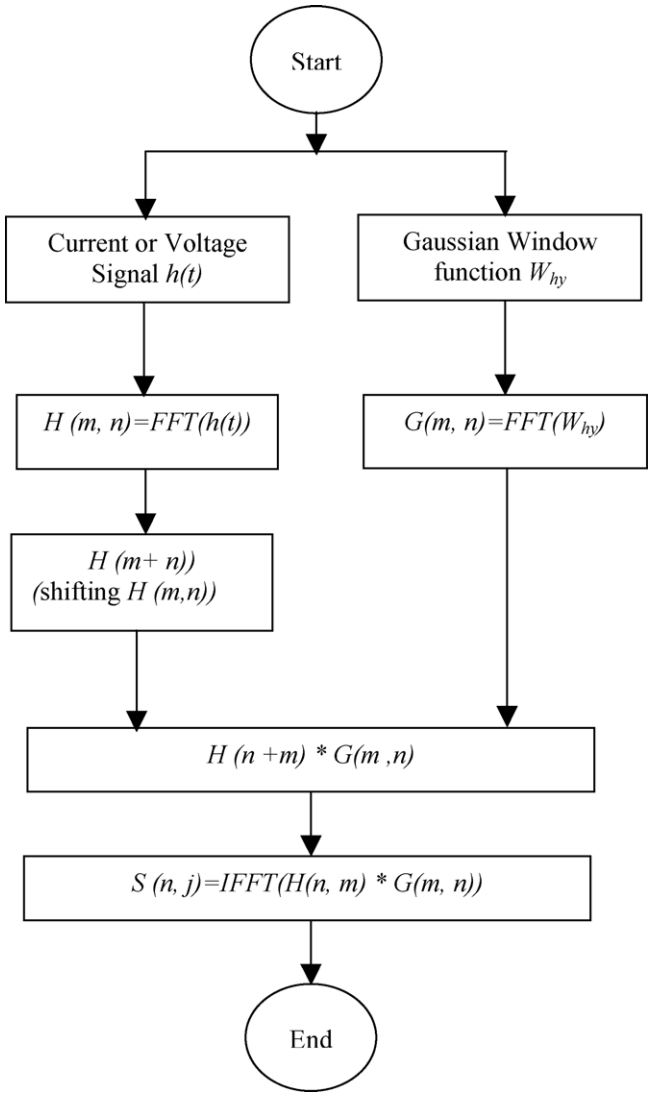

Fig. 2. Flow chart for HS transform.

and

$$sd = std\{abs(hs_f)\} \quad (12)$$

where hs_f the HS-transform coefficient is for one cycle ahead of fault inception and hs_n is the HS-transform coefficients for one cycle before the inception of the fault. For faulted phase identification, simulations are carried out for faults at intervals of 10 km from the sending end for a total line length of 300 km. For each of these fault locations inception angle (δ), fault resistance (R_f) and source impedance (Z_S) are varied to provide the change in

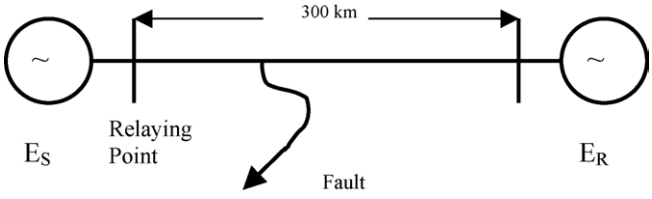

Fig. 3. Transmission line model.

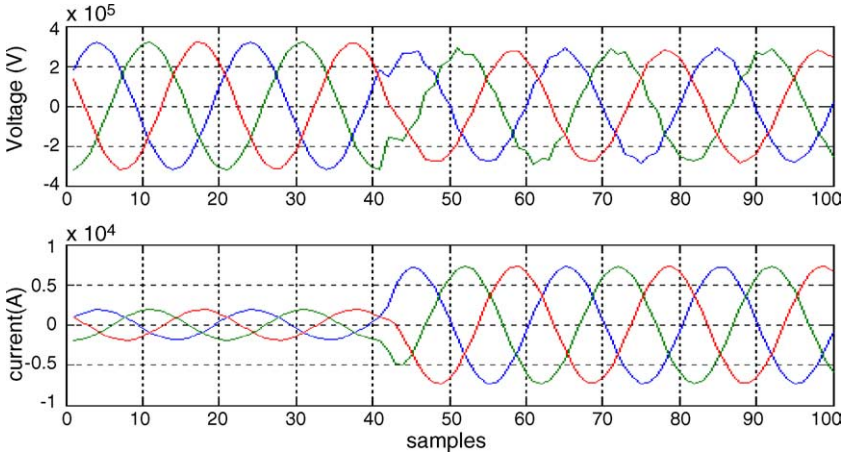

Fig. 4. Fault voltage and current signal for three-phase fault.

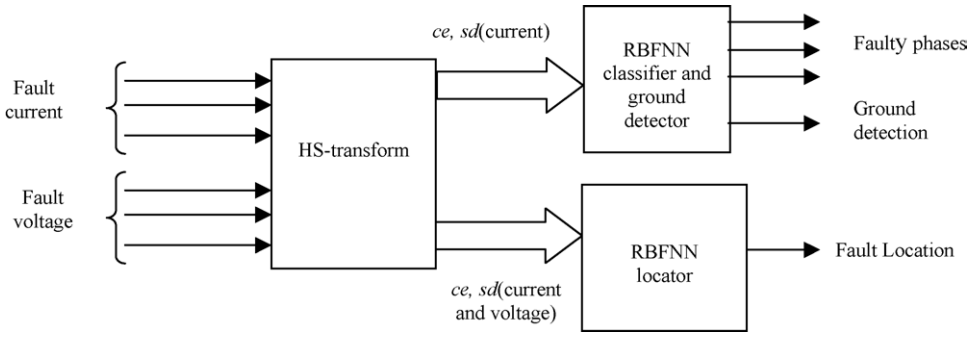

Fig. 5. Protection scheme for proposed method.

energy and standard deviation as presented in Tables 1 and 2. From the tables, it is seen that the faulted phases exhibit high output in the form of change in energy (ce) and standard deviation (sd) in comparison to the un-faulted phases.

For a line-to-line ground (LG) type, it is found from Tables 1 and 2 that the change in energy ce depends on the magnitude of the fault resistance, R_f, the value of ce is less for higher values of R_f. It is found from these tables that the current

Table 1
Change in energy (ce) and sd values for different faults (R_f = 20 Ω, fault at 10%, inception angle 180°, source impedance Z_S = 5 + j30 Ω)

Fault	*a*		*b*		*c*	
	ce_a	sd_a	ce_b	sd_b	ce_c	sd_c
LG						
ag	**49.6137**	**0.6269**	3.3263	0.0698	1.0416	0.0481
bg	1.7655	0.0859	**24.9729**	**0.3148**	3.1497	0.0920
cg	2.1833	0.0592	1.0604	0.0538	**34.9404**	**0.5415**
LLG						
abg	**49.7764**	**0.6724**	**18.9028**	**0.2907**	2.0117	0.0610
bcg	3.3505	0.0703	**36.7778**	**0.4392**	**43.9432**	**0.6116**
cag	**42.5899**	**0.5139**	2.4216	0.0841	**24.9239**	**0.4324**
LL						
ab	24.2053	**0.3070**	**22.2882**	**0.2856**	0.0001	0.0350
bc	0.0001	0.0350	**11.5396**	**0.2076**	**10.1772**	**0.2003**
ca	**26.7541**	**0.3909**	0.0001	0.0350	**28.0509**	**0.4028**
LLL						
abc	**28.3546**	**0.3984**	**19.6354**	**0.3125**	**22.3698**	**0.3678**
LLLG						
abcg	**33.7419**	**0.4424**	**16.2684**	**0.2178**	**23.1498**	**0.3767**

Bold values show the faulted phase.

Table 2
Change in energy (ce) and sd values for different faults (R_f = 200 Ω, fault at 30%, inception angle 180°, source impedance Z_S = 6 + j36 Ω)

Fault	*a*		*b*		*c*	
	ce_a	sd_a	ce_b	sd_b	ce_c	sd_c
LG						
ag	**15.8385**	**0.2117**	0.2464	0.0396	0.0230	0.0378
bg	0.9986	0.0647	**11.2101**	**0.1739**	1.1876	0.0647
cg	0.4431	0.0475	0.2272	0.0442	**14.9927**	**0.2370**
LLG						
abg	**16.4559**	**0.2231**	**8.9539**	**0.1491**	0.1174	0.0415
bcg	0.2905	0.0323	**11.7237**	**0.1727**	**12.5895**	**0.1969**
cag	**13.4441**	**0.1825**	0.4681	0.0559	**15.3726**	**0.2517**
LL						
ab	**9.9518**	**0.1473**	**8.1618**	**0.1281**	0.0000	0.0350
bc	0.0000	0.0350	**8.2121**	**0.1577**	**7.1622**	**0.1526**
ca	**13.1622**	**0.1526**	0.0001	0.0350	**12.3702**	**0.1854**
LLL						
abc	**12.3698**	**0.1759**	**10.2365**	**0.1548**	**9.3687**	**0.1987**
LLLG						
abcg	**13.4585**	**0.1874**	**8.5023**	**0.1370**	**12.1127**	**0.2046**

Bold values show the faulted phase.

signals in the faulted phases exhibit greater ce and standard deviation values in comparison to the un-faulted phases. Here ce_a, ce_b, ce_c represent change in energy and sd_a, sd_b, sd_c represent standard deviation in *a*, *b* and *c* phases, respectively.

4.2. Classification using radial basis function neural network (RBFNN)

Even if HS-transform gives information regarding the faulty phase involved, the RBFNN classifier is used to classify faults in the proposed method to overcome the error due to assigning threshold value to the parameters for fault identification including all operating conditions. After feature extraction using HS-transform, RBFNN is used to detect the faulty phase or multiple phases involving fault. The RBFNN [14] used here has an input layer, a hidden layer consisting of Gaussian node function, a set of weights *W*, to connect the hidden layer and output layer. Let x be the input vector $x = (x_1, x_2, \ldots, x_D)^{\mathrm{T}}$, where D represents input dimension. The output vector $o = (o_1, o_2, \ldots, o_N)^{\mathrm{T}}$, where N is the numbers of output node. For P training patterns, RBFNN approximates the mapping from the set of input $X = \{x(1), x(2), \ldots, x(P)\}$, to the set of outputs, $O = \{o(1), o(2), \ldots, o(P)\}$. For an input vector $x(t)$, the output of jth output node produced by an RBF is given by

$$o_j(t) = \sum_{i=1}^{m_{\mathrm{tot}}} w_{ij}\phi_i(t) = \sum_{i=1}^{m_{\mathrm{tot}}} w_{ij} e^{\frac{-||x(t) - \mathrm{c}_i||}{2\sigma_i}} \tag{13}$$

where c_i is the center of the 'i'th hidden node, σ_i is the width of the 'i'th center, and m_{tot} is the total number of hidden nodes.

If output of the hidden neurons, by vector notation

$$\varphi = (\phi_1(t), \phi_2(t), \ldots, \phi_{\mathrm{tot}}(t)) \tag{14}$$

and weight vector

$$w_j = (w_{1j}, w_{2j}, \ldots, w_{\mathrm{tot}j})$$

RBFNN output can be written as

$$o_j = w_j\varphi^{\mathrm{T}} \tag{15}$$

In our implementation these sets of centers are trained with *K*-means clustering approach, where the centers are initially defined as the first training m_{c} inputs that correspond to a specific class c. The center vector is given by

$$C_{\mathrm{c}}(i = 0) = \{x(c_1), x(c_2), \ldots, x(c_{m_{\mathrm{c}}})\} \tag{16}$$

At each iteration i, following a new input $x(i)$ is presented, the distance for each of the centers is denoted by

$$\rho_j(i) = ||x(i) - c_{j(i-1)}||, \quad \text{where } j = 1, 2, \ldots, m_{\mathrm{c}} \tag{17}$$

The kth center is updated by the following equation:

$$C_k(i) = C_k(i-1) + \alpha|\rho_k(i)| \tag{18}$$

where k that is chosen as the k that minimizes $\rho_j(i)$, as

$$k = \arg(\min(\rho_j(i))) \tag{19}$$

and α is the learning rate.

The width associated with the kth center is adjusted as

$$\sigma_k(i) = \sqrt{\frac{1}{N_a}\sum_{j=1}^{N_a} ||C_k(i) - C_j(i)||^2} \tag{20}$$

where N_a is the hidden neurons.

The weights of the RBF classifier can be trained using the linear recursive lease square (RLS) algorithm. The RLS is employed here since it has a much faster rate of convergence compared to the gradient search and least means square (LMS) algorithms.

$$k(i) = \frac{P(i-1)\varphi^{\mathrm{T}}(i)}{\lambda + P(i-1)\varphi^{\mathrm{T}}(i)} \tag{21}$$

$$w_j = w_j(i-1) + k(i)[d_j(i) - w_j(i-1)\varphi^{\mathrm{T}}(i)] \tag{22}$$

$$P(i) = \frac{1}{\lambda}[P(i-1) - k(i)\varphi(i)P(i-1)] \tag{23}$$

where λ is real number between 0 and 1, $P(0) = a^{-1} I$, and a is a small positive number and $w_j(0) = 0$.

The computational steps involved in implementing of RBFNN for fault classification are:

1. for each class c initial centers are first input sets that is $m_{\mathrm{c}} = m_{\mathrm{init}}$ (initialization);
2. train the RBFNN using current set of centers to get cross validation error for class c, $e = \{e_1, e_2 \ldots, e_{N_{\mathrm{c}}}\}$ (clustering of centers);
3. e_{m} (mean(e)) $\leq e_{\mathrm{target}}$ that is e_{m} has not decreased by 0.15% over last iteration, go to step 5 (convergence test);
4. add e_{inc} centers to N_{c} classes with highest error, to get a new m, then go to step 2;
5. the RBFNN is used with the one with the current m.

The learning rate of the RBFNN is 0.1 and the center and the weights are updated in every iteration that is by new training input to the RBFNN. Here only fault current signal is considered for feature extraction. Six inputs to the RBFNN fault classifier consisting of ce(i) and sd(i) values of all the three phases ('i' represents only current signal) are presented to the RBFNN and correspondingly three outputs are generated from the RBFNN, which gives the faulty phases involved. The RBFNN architecture for fault classification is shown in Fig. 6.

The RBFNN consists of three outputs representing 'a', 'b', 'c', phases. During training these outputs are assigned '1' or '0' considering whether the fault is involved with that phase or not. For example, 'abg' fault case the output will be assigned '1 1 0'. The training set include data (ce and sd) for 5, 15, 25, 35, 45, 55, 65, 75, 85, 95% fault location for different fault inception angles, fault resistance,different source impedance for 10 types of faults (ag, bg, cg, abg, bcg, cag, ab, bc, ca, abc, abcg). The flow chart for fault classification is shown in Fig. 7.

The performance of the RBFNN is tested for ce and sd values of different faults with varying location and fault resistance. Tables 3–6 present some of the classification results for faulted transmission line. Table 3 shows the performance of RBFNN

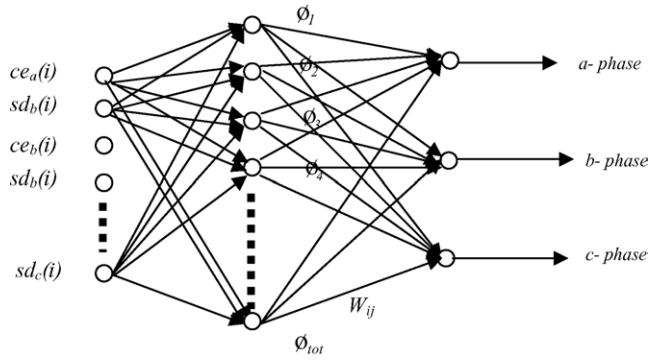

Fig. 6. RBFNN architecture for fault classification.

for 10% of the line and 45° inception angle for $R_f = 20$ and 200 Ω. The respective values in *a*, *b*, *c* columns for 'ab' case with $R_f = 20$ Ω, $a = 1.0098$, $b = 0.9947$, $c = 0.0298$ depicts the phases involved with the fault are '*a*' and '*b*' only. The classification

Table 3
Fault at 10% of line with 45° inception angle

Fault type	$R_f = 20$ Ω			$R_f = 200$ Ω		
	a	*b*	*c*	*a*	*b*	*c*
ag	0.9995	0.0025	0.0321	0.9987	0.0125	0.0241
bg	0.0325	1.0012	0.0125	0.9847	0.0541	0.0287
cg	0.0124	0.0354	1.0035	0.0354	0.0412	1.0036
abg	1.0048	0.9968	0.0014	1.0003	0.9974	0.0254
bcg	0.0036	1.0051	0.9874	0.0025	0.9964	0.9984
cag	1.0012	0.0041	1.0065	1.0041	0.0069	1.0954
ab	1.0098	0.9947	0.0298	1.0089	1.0074	0.0541
bc	0.0036	1.0051	0.9857	0.0041	0.9874	0.9968
ca	0.9945	0.0054	1.0087	1.0069	0.0654	1.0658
abc	1.0052	0.9998	0.9999	1.0023	0.9986	0.9979
abcg	1.0095	0.9991	0.9984	0.9948	0.9874	1.0019

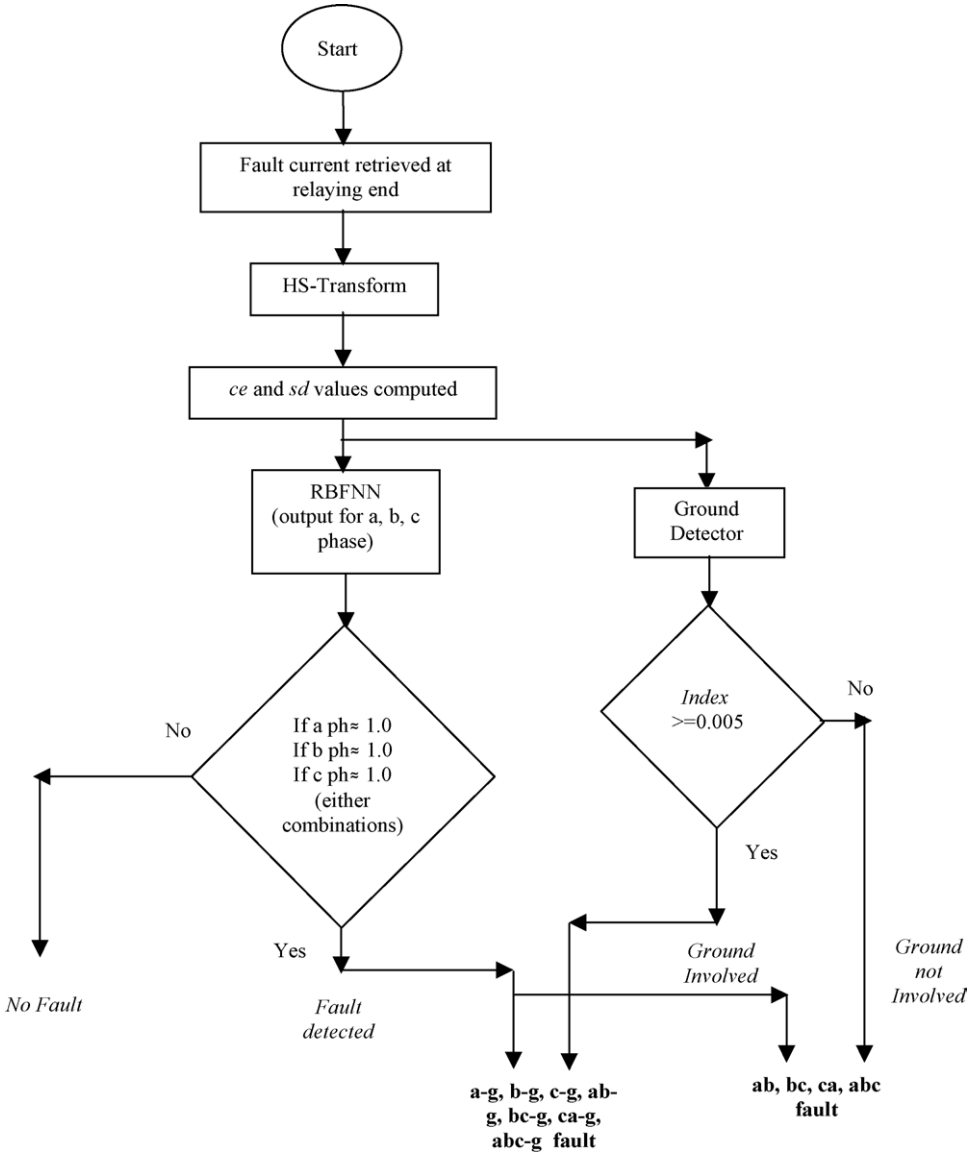

Fig. 7. Flow chart for fault classification.

Table 4
Fault at 30% of line with 60° inception angle

Fault type	$R_f = 20\ \Omega$			$R_f = 200\ \Omega$		
	a	*b*	*c*	*a*	*b*	*c*
ag	1.0025	0.0002	0.0013	0.9995	0.0026	0.0014
bg	0.0041	1.0098	0.0054	0.9987	0.0036	0.0254
cg	0.0254	0.0369	1.0008	0.0256	0.0036	1.0095
abg	1.0056	0.9995	0.0024	1.0096	0.9996	0.0025
bcg	0.0089	1.0009	1.0004	0.0012	0.9956	1.0236
cag	0.9996	0.0365	0.9996	1.0006	0.0065	0.9954
ab	1.0025	0.9968	0.0214	1.0006	1.0068	0.0036
bc	0.0006	0.9985	0.9965	0.0036	1.0069	1.0063
ca	1.0548	0.0698	1.0057	0.9958	0.0365	0.9968
abc	1.0028	0.9965	1.0026	0.9947	0.9968	0.9998
abcg	1.0026	1.0058	1.0008	0.9965	1.0045	0.9968

Table 5
Fault at 50% of line with 90° inception angle

Fault type	$R_f = 20\ \Omega$			$R_f = 200\ \Omega$		
	a	*b*	*c*	*a*	*b*	*c*
ag	1.0089	0.0045	0.0125	0.9989	0.0126	0.0123
bg	0.0214	1.0254	0.0654	0.9954	0.0254	0.0058
cg	0.0047	0.0096	1.0025	0.0214	0.0236	0.9954
abg	1.0048	0.9987	0.0125	1.0258	0.9965	0.0036
bcg	0.0012	1.0857	0.9954	0.0415	0.9854	1.0254
cag	0.9995	0.0254	0.9914	1.0032	0.0052	1.0063
ab	1.0025	0.9912	0.0041	1.0897	1.0036	0.0213
bc	0.0032	0.9965	0.9912	0.0024	0.9863	0.9995
ca	1.0065	0.0354	1.0069	1.0025	0.0032	1.0069
abc	0.9996	0.9994	1.0058	1.0023	0.9948	1.0054
abcg	1.0056	1.0002	1.0036	0.9968	1.0025	0.9997

approach takes a particular phase to be involved with fault if its corresponding values greater than a threshold value of 0.5 else it categorizes the phase to be 'undisturbed'. Similarly Table 4 provides the fault classification results for different faults at 30% of line with 60° inception angle. Also Table 5 provides the fault classification results for different faults at 50% of line with 90° inception angle where as Table 6 presents fault classification at 70% of line with 30° inception angle. The RBFNN has been trained by 3000 sets of data which comprises ce and sd for faulted

Table 6
Fault at 70% of line with 30° inception angle

Fault type	$R_f = 20\ \Omega$			$R_f = 200\ \Omega$		
	a	*b*	*c*	*a*	*b*	*c*
ag	1.0095	0.0023	0.00254	0.9987	0.0254	0.0036
bg	0.0014	1.0001	0.0025	0.9994	0.0058	0.0254
cg	0.0065	0.0045	1.0001	0.0254	0.0036	1.0058
abg	1.0048	0.9987	0.0012	1.0025	0.9925	0.0012
bcg	0.0125	1.0024	1.0025	0.0254	0.9958	1.0026
cag	0.9998	0.0125	0.9968	1.0032	0.0036	1.0254
ab	1.0012	0.9998	0.0125	1.0045	10.365	0.0025
bc	0.0254	0.9945	0.9941	0.0145	0.9968	0.9958
ca	1.0025	0.0654	1.0254	0.9995	0.0036	1.0025
abc	0.9945	1.0023	1.0045	1.0254	0.9991	0.9967
abcg	0.9985	1.0025	1.0014	0.9968	1.0065	0.9995

Table 7
Index values for fault at 10% of the line at different fault resistance

Fault type	Index ($R_f = 0\ \Omega$)	Index ($R_f = 200\ \Omega$)
ag	0.0365894	0.1258974
abg	0.0251478	0.1548695
ab	0.0000005	0.0000003
abcg	0.4587925	0.4258974

current signals of every kind of fault at various locations, fault resistance, and inception angle. Observation of all test results ascertains that the RBFNN performs excellent even at different inception angles, fault location and fault resistance and pre-fault loading conditions.

4.3. Ground detection

Usually RBFNN may not give ground detection properly. Therefore ground detection task is not included in the RBFNN classifier. For detecting the involvement of ground, an index is proposed as given below:

$$\text{index} = \frac{\min(\text{ce}_a, \text{ce}_b, \text{ce}_c)}{\max(\text{ce}_a, \text{ce}_b, \text{ce}_c)} \tag{24}$$

The ground detection is carried out in conjunction with the RBFNN classification. Test result showing the values of index for ag, abg, ab, abcg faults at 10% of line and fault resistances of 0 and 200 Ω are given in Table 7. When the index value exceeds the threshold value of 0.005, it indicates the involvement of fault with ground. This value of index has been tested for different types of fault with various operating conditions.

5. Fault location using RBFNN

Once the fault is classified, the control unit activates the fault locating RBFNN to locate the fault. Here RBFNN with RLS algorithm is used to build the fault locator. In this case the learning rate of the RBFNN is 0.1 and the center and the weights are updated in every iteration that is by new training input to the RBFNN. Here for fault location both voltage and current signal are considered and tuned through HS-transform to yield change in energy and standard deviation. There are 12 inputs consisting of 6 for current signal (ce(i) and sd(i) for each phase) and 6 for voltage signal (ce(v) and S.D.(v) for each phase) are fed to the RBFNN and correspondingly one output is generated from the RBFNN, which is the distance of the fault from the relaying point. The RBFNN has been trained using 3000 sets of data that comprises ce and sd for faulted current and voltage signals of every kind of fault at various locations (15, 25, 35, 45, 55, 65, 75, 85, 95% of transmission line), fault resistance, and inception angle. The RBFNN architecture for fault location determination is given in Fig. 8.

The percentage error is computed as

$$\text{error}\,(\%) = \frac{|\text{actual distance} - \text{calculated distance}|}{\text{protected line length}} \times 100 \tag{25}$$

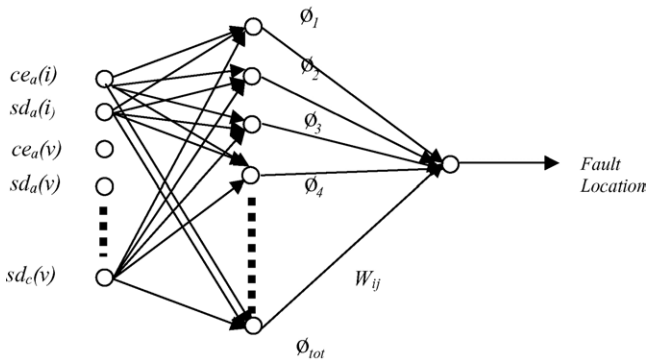

Fig. 8. RBFNN architecture for fault location.

Table 8
Fault location for L-G faults

Distance (%)	Fault resistance (R_f)	Error (%)
10	0	1.01
	200	0.89
30	0	0.99
	200	1.12
50	0	1.11
	200	1.03
70	0	0.99
	200	0.96
90	0	1.00
	200	1.06

Table 9
Fault location for LL-G faults

Distance (%)	Fault resistance (R_f)	Error (%)
10	0	1.23
	200	1.11
30	0	1.26
	200	1.11
50	0	1.02
	200	1.12
70	0	1.89
	200	0.96
90	0	1.00
	200	1.23

Table 10
Fault location for LL faults

Distance (%)	Fault resistance (R_f)	Error (%)
10	0	1.23
	200	1.23
30	0	0.98
	200	1.03
50	0	1.02
	200	0.98
70	0	0.97
	200	1.03
90	0	0.99
	200	1.08

Table 11
Fault location for LLL faults

Distance (%)	Fault resistance (R_f)	Error (%)
10	0	0.99
	200	1.32
30	0	1.08
	200	1.01
50	0	0.96
	200	1.26
70	0	0.94
	200	1.12
90	0	1.11
	200	1.22

Table 12
Fault location for LLL-G faults

Distance (%)	Fault resistance (R_f)	Error (%)
10	0	1.36
	200	1.41
30	0	0.98
	200	1.12
50	0	1.45
	200	1.36
70	0	0.96
	200	1.11
90	0	0.98
	200	1.02

The location error shown in Tables 8–12 for 10, 30, 50, 70, 90% and L-G, LL-G, LL, LLL, LLL-G fault with fault resistance R_f from 0 to 200 Ω. The location error for 10% of line with L-G fault with $R_f = 0\ \Omega$ is 1.01% and with $R_f = 200\ \Omega$ is 0.89%. Likewise Tables 9–12 show the percent error for LL-G, LL, LLL and LLL-G fault, respectively. The error is the least in case of L-G fault that is 0.89% at 10% of line and goes up to 1.89% in case of LL-G fault at 70% of the transmission line.

6. Conclusion

An efficient fault classification and location determination using HS-transform and RBFNN is presented in this paper. HS-transform based time frequency analysis is used for feature extraction by computing the standard deviation and change in energy at varying window. After feature extraction, RBFNN is used for faulty phase detection and classification. The change in energy and standard deviation are the input to the RBFNN, which provides the output for classification. The output is very nearly '1' for faulty phase and '0' for un-faulted phase. The classification result given in Tables 3–6 shows the effectiveness of RBFNN for accurately identifying the faulted phase. Once the faulty phases are identified, the fault distance can be computed by RBFNN. RBFNN locator gives the distance of the fault from the relaying point and the error calculated for all kinds of faults is below 2%. The trained networks are capable of providing fast

and precise classification and location for different types faults with various inception angle and fault resistance.

References

[1] O.A.S. Youssef, New Algorithms for phase selection based on wavelet transforms, IEEE Trans. Power Deliv. 17 (2002) 908–914.

[2] O.A.S. Youssef, Online applications of wavelet transform to power system relaying, IEEE Trans. Power Deliv. 18 (4) (2003) 1158–1165.

[3] O.A.S. Youssef, Combined Fuzzy-Logic wavelet based fault classification for power system relaying, IEEE Trans. Power Deliv. 19 (2) (2004) 582–589.

[4] A.H. Osman, O.P. Malik, Transmission line protection based on wavelet transform, IEEE Trans. Power Deliv. 19 (2) (2004) 515–523.

[5] F. Martin, J.A. Aguado, Wavelet based ANN approach for Transmission line protection, IEEE Trans. Power Deliv. 18 (4) (2003) 1572–1574.

[6] D. Chanda, N.K. Kishore, A.K. Sinha, A wavelet multi-resolution analysis for location of faults on transmission lines, Electr. Power Energy Syst. 25 (2003) 59–69.

[7] Hong-Tzer Yang, Chiung-Chou Liao, A de-noising scheme for enhancing wavelet-based power quality monitoring system, IEEE Trans. Power Deliv. 16 (3) (2001 July) 353–360.

[8] R.G. Stockwell, L. Mansinha, R.P. Lowe, Localization of the complex spectrum: the S-transform, IEEE Trans. Signal Process 44 (1996) 998–1001.

[9] G. Livanos, N. Ranganathan, J. Jiang, Heart sound analysis using the S-transform, IEEE Comp. Cardiol. 27 (2000) 587–590.

[10] R.G. Stockwell, L. Mansinha, R.P. Lowe, Localization of complex spectrum: the S-transform, J. Assoc. Expl. Geophys. XVII (July (3)) (1996) 99–114.

[11] P.K. Dash, B.K. Panigrahi, G. Panda, Power quality analysis using S-transform, IEEE Trans. Power Deliv. 18 (2003) 406–411.

[12] C.R. Pinnegar, Lalu. Mansinha, The S-transform with windows of arbitrary and varying window, Geophysics 68 (2003) 381–385.

[13] M. Gauda, M.A. Salama, M.R. Sultam, A.Y. Chikhani, Power quality detection and classification using wavelet multi-resolution signal decomposition, IEEE Trans. Power Deliv. 14 (1999) 1469–1476.

[14] T. McConaghy, H. Lung, E. Bosse, V. Vardan, Classification of audio radar signals using Radial Basis Function Neural Network, IEEE Trans. Inst. Meas. 52 (6) (2003 December) 1771–1779.

P.K. Dash (SM' 1990) is working as Director College of Engineering, Bhubaneswar, India. Earlier he was a professor in the Faculty of Engineering, Multimedia University, and Cyberjaya, Malaysia. He also served as a professor of electrical engineering and chairman, center for intelligent systems, National Institute of Technology, Rourkela, India for more than 25 years. Dr. Dash holds D.Sc., Ph.D., M.E., and B.E. degrees in electrical engineering and had his post-doctoral education at the University of Calgary, Canada. His research interests are in the area of power quality, FACTS, soft computing, deregulation and energy markets, signal processing, and data mining and control. He had several visiting appointments in Canada, USA, Switzerland, and Singapore. To his credit he has published more than 150 International Journal papers and nearly 100 in International conferences. Prof. Dash is a fellow of the Indian National Academy of Engineering and senior member of the IEEE, and fellow of Institution of Engineers, India.

S.R. Samantaray is pursuing his Ph.D. in the Department of Electronics and Communication Engineering, National Institute of Technology, Rourkela, in the area of power system protection. His major interest includes intelligent protection, digital signal processing, soft computing, FACTs. Graduated in electrical engineering (Hons.), he worked in TATA group in the area of power system, industrial automation and instrumentation.

Ganapati Panda received Ph.D. degree in digital signal processing from IIT, Kharagpur, India, and post doctorate from University of Edinburgh, UK, in 1982 and 1984–1986, respectively. He has published more than 160 papers in referred research journals and conferences. He carries out research work in the field of DSP, soft-computing and digital communication. He is a fellow of INAE and National Academic of Science, India. Presently he is working as a professor in the Department of Electronics & Instrumentation Engineering at NIT, Rourkela, India.